AIMS Mathematics, 11(8): 26538–26567.
DOI:10.3934/math.20261064
Received: 15 June 2026
Revised: 28 July 2026
Accepted: 7 August 2026
Published: 25 August 2026

https://www.aimspress.com/journal/Math

Research article

Parameter optimization and benchmark verification of a local radial basis function collocation method for transient heat conduction in multilayer thin-walled structures

Tao Ding* **and Yuanjian Lin**

School of Intelligent Construction, Wuxi Taihu University, Wuxi 214064, China

* **Correspondence:** Email: dingt@wxu.edu.cn.

Abstract: This paper calibrates and verifies a local radial basis function collocation method (LRBFCM) for transient heat conduction in multilayer thin-walled structures. The discrete system is stated in full, including the row construction for interior, Dirichlet, Neumann, and interface nodes and the load vector required by inhomogeneous Dirichlet data. The method is verified against the exact series solution of the single-layer benchmark through error norms and spatial and temporal convergence studies, together with a steady series-resistance check of the interface treatment. A fixed-domain calibration expresses the shape parameter nondimensionally as $c = \beta h$ and identifies the wall thickness as a candidate length scale for the tested configuration. On the tested single-layer node set, later-time accuracy and early-time undershoot are found to vary in opposite directions as the local stencil is widened, and documented finite element runs show a corresponding contrast between element orders. Multilayer simulations of two- and five-layer composite walls illustrate the calibrated scheme.

Keywords: local radial basis function collocation method; meshless method; transient heat conduction; shape parameter calibration; discrete maximum principle; multilayer thin-walled structure
Mathematics Subject Classification: 65M70, 65M12, 80M22

1. Introduction

Traditional mesh-based methods, including the finite element and finite difference methods, remain widely used for heat conduction and composite-media simulations [1–3]. Meshless methods instead use scattered-node interpolation. Global radial basis function (RBF) collocation has a concise formulation [4, 5], and its interpolation theory is established for conditionally positive-definite (CPD) kernels [6, 7]. The method nevertheless produces dense systems, and conditioning can deteriorate as the basis is flattened or the problem is enlarged. Local formulations replace the global dense coupling

with sparse stencil rows.

Early variants used symmetry or modified collocation formulations. Zhang [8] and Chen [9] described Hermite collocation and the modified Kansa method (MKM), respectively. RBF-generated finite differences (RBF-FD) and local RBF collocation [10–12] construct sparse rows from local stencils. Subsequent studies applied local, stabilized, and adaptive RBF collocation to elastic-wave, incompressible-flow, and elliptic-interface problems [13–15]. Localized RBF formulations were later extended to transient elastic-wave band structures, phase-field evolution, and long-time nonlinear heat conduction [16–18]. Space-time RBF schemes addressed three-dimensional anisotropic heat conduction, Hausdorff-derivative heat equations, and coupled thermo-mechanical analysis [19–21]. Recent related collocation developments for transient heat conduction include localized Fourier, arbitrary-order, and hybrid schemes [22–24]. For boundary derivatives, Zheng et al. [25] developed three treatments for stable normal-derivative evaluation, including the direct method used here. A subsequent study [26] evaluated the derivative through a finite-difference construction with a fictitious node.

The selection of the multiquadric shape parameter has itself received sustained attention. Rippa [27] proposed a leave-one-out cross-validation criterion, Fasshauer and Zhang [28] examined its extension to iterated approximate moving least squares, and Schaback [29] established the trade-off between attainable accuracy and conditioning, including the severe ill-conditioning associated with flattened bases. For localized schemes, Zheng et al. [30] proposed selecting the shape parameter through a test differential equation with a known solution. The calibration reported in Section 3.4 is instead benchmark-based and examines the length scale followed by the optimum. What remains insufficiently systematic is calibration for *thin-walled and layered interface* configurations, where the aspect ratio fixes the nodes available across the thickness and the stencil can straddle material discontinuities. That is the gap addressed here.

This study does not propose a new discretization principle. Its subject is the choice of parameters within the standard local multiquadric RBF (MQ-RBF) collocation scheme, applied to transient heat conduction in multilayer thin-walled structures—a configuration in which the extreme aspect ratio and the internal material interfaces jointly restrict the admissible node distribution, stencil size, and shape parameter, so that the parameter choices cannot be inherited from the literature on smooth domains.

The central numerical observation is that, for the single-layer configuration and early-time window tested, accuracy per degree of freedom and absence of an early undershoot can vary in opposite directions as the local stencil is widened. On the fixed node set, a 3×3 collocation stencil showed no negative value above the double-precision floor for the usable shape parameters, whereas the selected wider-stencil setting produced a negative excursion and a lower listed error. The corresponding finite element tests show a related contrast between the tested four-node linear and eight-node quadratic formulations. Changes in the sign structure of the assembled discrete operators are one possible explanation, but the present data do not isolate that mechanism or establish an equivalence between the two method families.

The specific contributions are (i) a numerical characterization of that trade-off in the tested single-layer configuration, including the separate effects of stencil size and shape parameter (Section 4.5); (ii) a fixed-domain calibration showing how the fitted optimum changes with nodal spacing and stencil size (Section 3.4); (iii) a complete statement of the discrete system, including the load vector required to impose inhomogeneous Dirichlet data and the flux-continuity rows at material interfaces, together

with the algorithm used for stencil selection (Section 4.1); and (iv) verification against the exact series solution of the single-layer problem, with error norms and spatial and temporal convergence studies, and a finite element comparison documenting the settings used in the controlled runs (Sections 4.3 and 4.4).

The structure of this paper is as follows: Section 2 states the collocation construction; Section 3 analyses node distribution, local point selection, the shape parameter, and thin-walled convergence; Section 4 states the discrete system, verifies it against the exact solution, reports the finite element comparison, and characterises the trade-off; Section 5 summarises conclusions and outlines future research directions.

2. Theory of the local RBF meshless collocation method

RBFs are a class of basis functions using Euclidean geometric distance as the variable, possessing advantages of simple form, independence from spatial dimension, and isotropy. Traditional RBFs can be classified into globally supported RBFs (GS-RBFs) and compactly supported RBFs (CS-RBFs). Table 1 presents several common GS-RBFs, where c is the shape parameter and r is the Euclidean distance. This study employs the multiquadric RBF (MQ-RBF) as the basis function.

Table 1. Common GS-RBFs.

Name	$\phi(r)$	CPD Order
Power spline (PS)	$r^{2k+1}, k \in \mathbb{N}$	$k+1$
Thin-plate spline (TPS)	$r^{2k}\ln(r), k \in \mathbb{N}$	$k+1$
Multiquadric (MQ)	$(r^2+c^2)^{1/2}$	1
Inverse MQ (IMQ)	$(r^2+c^2)^{-1/2}$	0
Gaussian	$\exp(-r^2/c^2)$	0

The CPD classifications in Table 1 follow the standard theory of CPD radial functions [6, 7].

The local RBF meshless collocation method is a local approach based on global RBFs. At every node, an RBF expansion is constructed from the surrounding stencil and then differentiated to obtain a difference-like operator row. Consider a second-order partial differential equation:

$$Lu(\mathbf{x}) = f(\mathbf{x}), \quad \mathbf{x} \in \Omega, \tag{2.1}$$

$$\mathcal{B}u(\mathbf{x}) = p_N(\mathbf{x}), \quad \mathbf{x} \in \Gamma_N, \tag{2.2}$$

$$u(\mathbf{x}) = p_D(\mathbf{x}), \quad \mathbf{x} \in \Gamma_D, \tag{2.3}$$

where $\mathbf{x} = [x, y]$ denotes the two-dimensional coordinate variables; Ω represents the interior solution domain; L is the interior differential operator (the symbol L is used in place of I so as not to be confused with the identity matrix); Γ_N denotes the second-kind (Neumann) boundary, on which $\mathcal{B}$ is the boundary differential operator; Γ_D denotes the first-kind (Dirichlet) boundary; and $p_N(\mathbf{x})$ and $p_D(\mathbf{x})$ are the prescribed Neumann and Dirichlet data. These boundary-type symbols are distinct from the face labels Γ_1–Γ_4 used for the heat-conduction geometry in Section 4.2.

On a local stencil, the RBF collocation method approximates the solution $u(\mathbf{x})$ by a linear combination of RBFs:

$$u(\mathbf{x}) = \sum_{j=1}^{n_e} \omega_j \phi(\mathbf{x}, \mathbf{x}_j), \tag{2.4}$$

where n_e is the number of local points ($n_e = 9$ unless stated otherwise; Sections 3.4 and 4.5 also examine $n_e = 5$, 13 and 21), $\mathbf{x}_j$ denotes each discrete point, ω_j is an RBF expansion coefficient, and $\phi(r) = \sqrt{r^2 + c^2}$ is the MQ kernel, with $r = \|\mathbf{x} - \mathbf{x}_j\|$ and shape parameter c.

Enforcing Eq (2.4) at every node $\mathbf{x}_k$ of the stencil gives the square interpolation system

$$\mathbf{\Phi}_{n_e \times n_e} \boldsymbol{\omega}_{n_e} = \mathbf{u}_{n_e}, \qquad \boldsymbol{\omega}_{n_e} = \mathbf{\Phi}^{-1}_{n_e \times n_e} \mathbf{u}_{n_e}. \tag{2.5}$$

Here $(\mathbf{\Phi}_{n_e \times n_e})_{kl} = \phi(\|\mathbf{x}_k - \mathbf{x}_l\|)$, $k, l = 1, \ldots, n_e$ is the local interpolation matrix and $\mathbf{u}_{n_e} = [u(\mathbf{x}_1), \ldots, u(\mathbf{x}_{n_e})]^T$. The MQ kernel is CPD of order one, as recorded in Table 1. The local Kansa-type implementation used here solves the unaugmented square system and checks each local matrix for numerical nonsingularity; no polynomial augmentation is used in the calculations reported below.

For simplicity, defining $\boldsymbol{\chi}^L_{n_e}(\mathbf{x}) = L\mathbf{\Theta}_{n_e}\mathbf{\Phi}^{-1}_{n_e \times n_e}$, $\boldsymbol{\chi}^{\mathcal{B}}_{n_e}(\mathbf{x}) = \mathcal{B}\mathbf{\Theta}_{n_e}\mathbf{\Phi}^{-1}_{n_e \times n_e}$, and $\boldsymbol{\chi}_{n_e}(\mathbf{x}) = \mathbf{\Theta}_{n_e}\mathbf{\Phi}^{-1}_{n_e \times n_e}$, where $\mathbf{\Theta}_{n_e} = [\phi(\|\mathbf{x} - \mathbf{x}_1\|), \ldots, \phi(\|\mathbf{x} - \mathbf{x}_{n_e}\|)]$, the partial differential equation can be rewritten as

$$Lu(\mathbf{x}) = \boldsymbol{\chi}^L_{n_e}(\mathbf{x})\mathbf{u}_{n_e} = f(\mathbf{x}), \tag{2.6}$$

$$\mathcal{B}u(\mathbf{x}) = \boldsymbol{\chi}^{\mathcal{B}}_{n_e}(\mathbf{x})\mathbf{u}_{n_e} = p_N(\mathbf{x}), \tag{2.7}$$

$$u(\mathbf{x}) = \boldsymbol{\chi}_{n_e}(\mathbf{x})\mathbf{u}_{n_e} = p_D(\mathbf{x}). \tag{2.8}$$

The vectors $\boldsymbol{\chi}^L(\mathbf{x})$ and $\boldsymbol{\chi}^{\mathcal{B}}(\mathbf{x})$ are local differentiation weights; they are distinct from the RBF expansion coefficients $\boldsymbol{\omega}_{n_e}$. By inserting zero elements at appropriate positions, these local rows are extended to global sparse rows acting on the $N \times 1$ global field vector $\mathbf{u} = [u(\mathbf{x}_1), \ldots, u(\mathbf{x}_N)]^T$. Relative to global RBF collocation, this construction replaces a dense global operator by sparse local rows and reduces the associated storage requirement.

Throughout, n_e denotes the number of nodes in the two-dimensional interior stencil and n_b the number of nodes in the one-dimensional stencil used on boundaries and interfaces; the two are distinct. Each numerical study states the values relevant to it, either locally or in its settings table. The MQ kernel is $\phi(r) = (r^2 + c^2)^{1/2}$ throughout. Its derivatives, needed for the boundary and Laplacian rows, are

$$\frac{\partial \phi}{\partial x_i} = \frac{x_i - x_{j,i}}{\sqrt{r^2 + c^2}}, \qquad \nabla^2 \phi = \frac{r^2 + 2c^2}{(r^2 + c^2)^{3/2}} \quad \text{in two dimensions.} \tag{2.9}$$

3. Parameter optimization strategies

The local radial basis function collocation method (LRBFCM) constructs sparse operator rows from points placed in the computational domain. Its accuracy and numerical conditioning depend on the node distribution, local point-selection strategy, stencil size, and shape parameter. This section examines those dependencies through numerical experiments.

3.1. Node distribution strategies

In collocation methods, node distribution can be classified into regular and irregular distributions. Figure 1 illustrates two different uniform distribution configurations in a 1×1 computational domain.

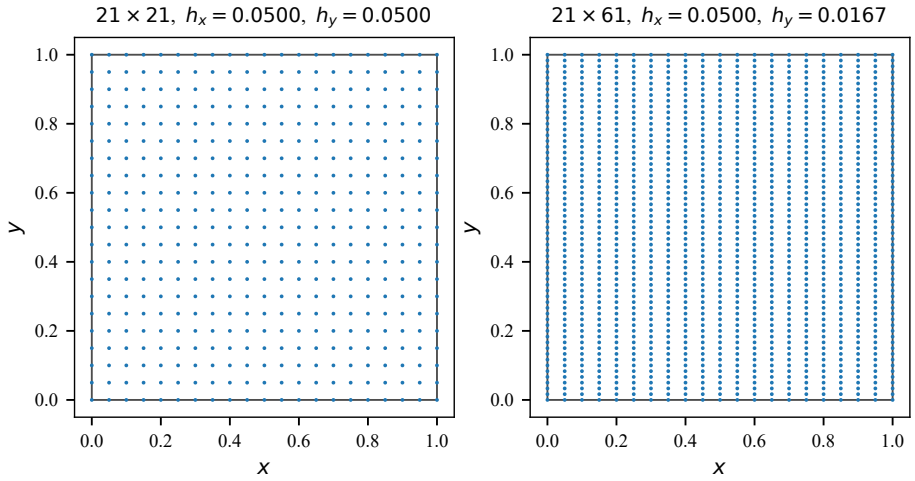

Figure 1. Regular node distributions in the unit square. Left: equal spacing in both directions. Right: the same 21 nodes across x but 61 along y, so that h_y is three times smaller than h_x and a nine-point stencil becomes strongly anisotropic. Axes are in the nondimensional coordinates of (3.1).

Consider the Poisson equation in a 1×1 computational domain:

$$\nabla^2 P(x, y) = 2e^{x+y}, \quad 0 \le x \le 1, \quad 0 \le y \le 1. \tag{3.1}$$

The boundary conditions are $g_1 = e^x$ $(y = 0)$, $g_2 = e^{x+1}$ $(y = 1)$, $g_3 = e^y$ $(x = 0)$, and $g_4 = e^{y+1}$ $(x = 1)$. The analytical solution is $P = e^{x+y}$. The maximum absolute error $Er = \max|\bar{P} - P|$ is used to evaluate computational accuracy, where $\bar{P}$ is the numerical solution and P is the analytical solution. The number of local points is set to nine.

In Table 2, the lowest errors at $c = 1$, 2, and 5 occur on the 21×31 grid. Increasing the node count in the y direction alone produces no systematic improvement: Most entries on the 21×41 to 21×61 grids are comparable to or larger than those on 21×31, with only a modest decrease at $c = 0.5$, and at $c = 5$ the most anisotropic grid produces a numerically singular local interpolation matrix.

Table 2. Numerical errors under different uniform distributions with various shape parameters. The entry marked—produced a numerically singular local interpolation matrix.

c	21×21	21×31	21×41	21×51	21×61
0.1	1.08	0.98	0.91	0.98	0.98
0.5	3.6×10^{-3}	2.6×10^{-3}	2.5×10^{-3}	2.5×10^{-3}	2.3×10^{-3}
1	1.3×10^{-4}	9.6×10^{-5}	1.5×10^{-4}	1.5×10^{-4}	1.5×10^{-4}
2	8.6×10^{-5}	6.3×10^{-5}	1.2×10^{-4}	1.0×10^{-4}	1.3×10^{-4}
5	1.0×10^{-4}	3.7×10^{-5}	1.3×10^{-4}	1.2×10^{-4}	—

Figure 2 shows the fixed-seed nonuniform cloud used in this test: 80 equally spaced boundary nodes and 361 uniformly sampled interior nodes in a 1×1 domain.

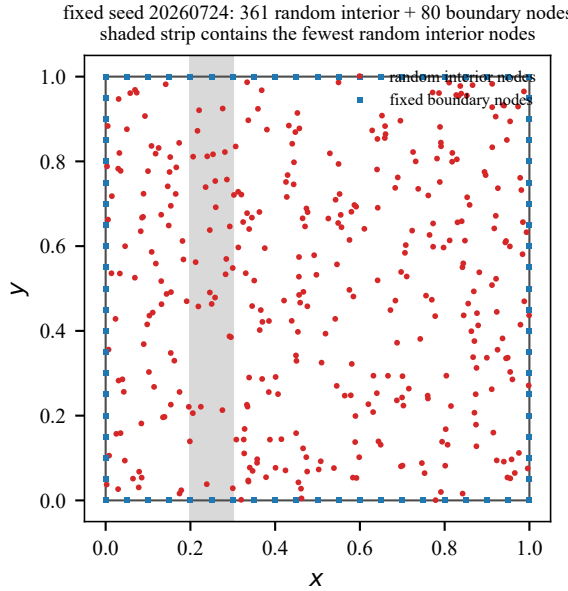

Figure 2. Fixed-seed nonuniform node cloud in the unit square (seed 20260724): 80 equally spaced boundary nodes; 361 uniformly sampled interior nodes. The shaded strip is the sparsest decile in x and illustrates the nonuniform local coverage.

The cloud contains 441 unique nodes and no duplicate points; its minimum pair distance is 2.55×10^{-3}, and its fill distance, estimated on a 101×101 sampling grid, is 8.80×10^{-2}. Thus duplicate nodes cannot explain the large errors in Table 3. Instead, the cloud combines nonuniform local coverage with local condition numbers that grow strongly with c. The error is non-monotone in c; its sampled minimum, 2.69×10^{-1} at $c = 0.5$, remains far above the 2.6×10^{-3} error on the 21×31 uniform grid at the same c (Table 2). This single fixed-seed realisation does not establish a distribution-free ranking; it supports using controlled, near-uniform spacing for the calculations below.

Table 3. Results on the fixed-seed nonuniform cloud in Figure 2; κ_2 denotes the matrix 2-norm condition number.

c	max absolute error	max local κ_2	global κ_2
0.1	7.62	3.77×10^{6}	3.14×10^{6}
0.5	2.69×10^{-1}	7.15×10^{10}	8.84×10^{6}
1	5.79×10^{-1}	9.49×10^{12}	6.12×10^{7}
2	1.19	1.78×10^{15}	1.26×10^{8}
5	2.27	1.01×10^{19}	1.16×10^{10}

3.2. Local point selection strategy

In thin-walled structures, especially heat-conduction problems in multilayer materials, continuous interface conditions between different materials often need to be considered, requiring boundary

derivative calculations. LRBFCM often produces significant errors in derivative calculations. To address this issue, the direct method is employed for solving second-kind (Neumann) boundary-condition problems.

Consider the same governing Eq (3.1) as in Section 3.1 but change the boundary condition at $y = 0$ to a second-kind (Neumann) condition:

$$\frac{\partial P}{\partial n} = -e^x, \quad y = 0, \quad 0 \le x \le 1. \tag{3.2}$$

A 31×31 node distribution is used, with shape parameter $c = 1$, interior stencil $n_e = 9$, and a one-dimensional boundary stencil of $n_b = 5$. The core idea of the direct method [25] is to select the interpolation nodes only along the grid line normal to the boundary (for the boundary $y = 0$, the y direction), physically reducing the two-dimensional derivative evaluation to a one-dimensional one and thereby achieving more accurate derivative results. Figure 3 illustrates the two different point selection methods.

In Figure 3, grey dots represent the full node set, the red square marks the boundary node under consideration, and green circles indicate the local nodes selected for it. Figure 4 shows the error distribution results of both methods.

Both panels use identical interpolation points and shape parameters and impose the same outward-normal convention. On $y = 0$, $\mathbf{n} = -\mathbf{e}_y$, so the exact data are $\partial P/\partial n = -e^x$. The direct method has a maximum absolute error of 6.89×10^{-5}, and the conventional nearest-point treatment has 5.43×10^{-4}, a ratio of 7.89 on this test.

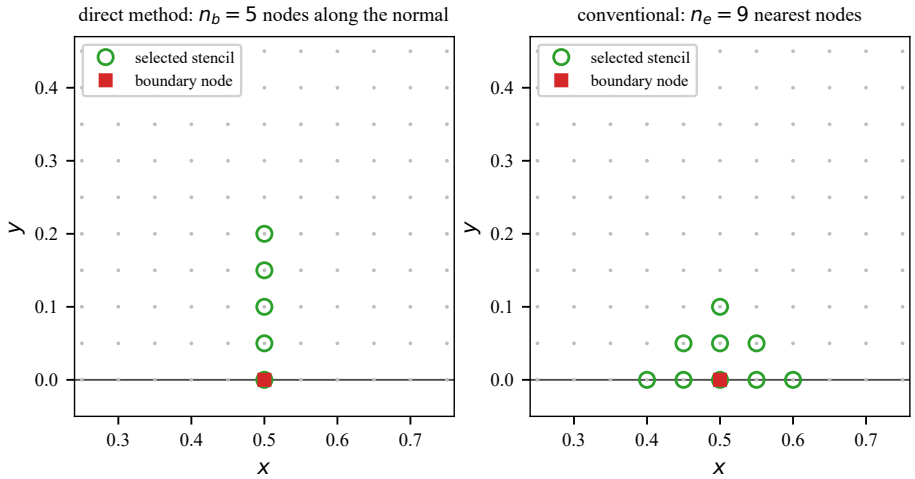

Figure 3. Stencil selection for a node on a second-kind boundary, drawn from the selection routine itself and illustrated for a node on the face $y = 0$—the boundary carrying the second-kind condition (3.2)—with $n_b = 5$. The direct method takes n_b collinear nodes along the inward normal, reducing the derivative to one dimension. The conventional choice of the n_e nearest nodes is one-sided and places five of the nine nodes (including the collocation node itself) on the boundary, which is why it approximates the normal derivative poorly.

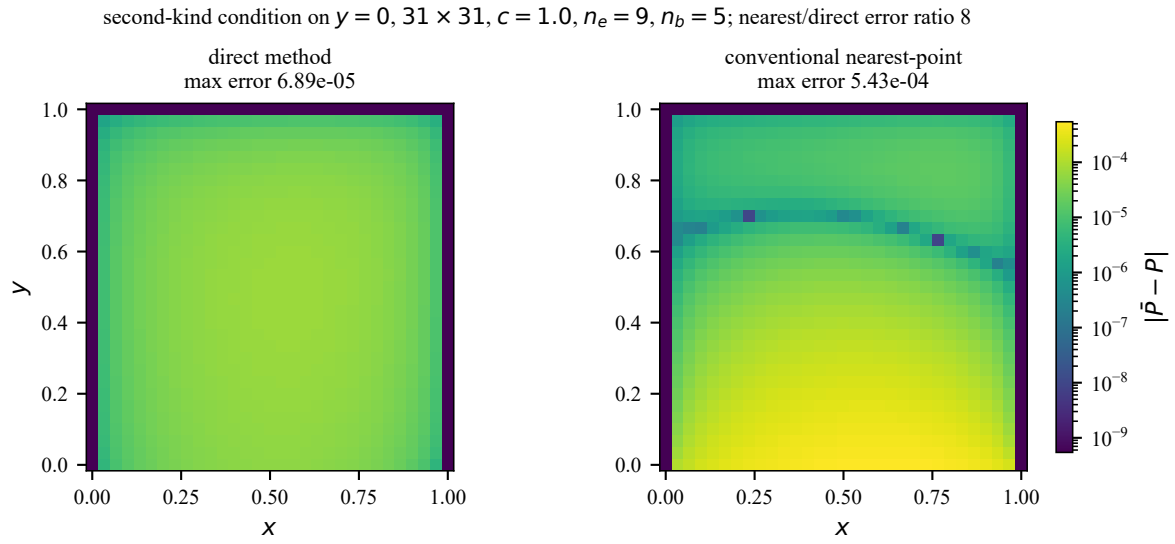

Figure 4. Absolute error field of the Poisson test problem (3.1) with the second-kind condition (3.2) on $y = 0$ for the two boundary-derivative treatments (31×31, $c = 1$, $n_e = 9$, $n_b = 5$). Both panels share the logarithmic colour scale. The error of the conventional treatment is concentrated on the boundary carrying the derivative condition.

3.3. Shape parameter selection

The shape parameter c significantly affects the computational accuracy of the MQ-RBF. Using a 31×31 node distribution as an example, computational errors under different shape parameters are investigated, with results shown in Figure 5.

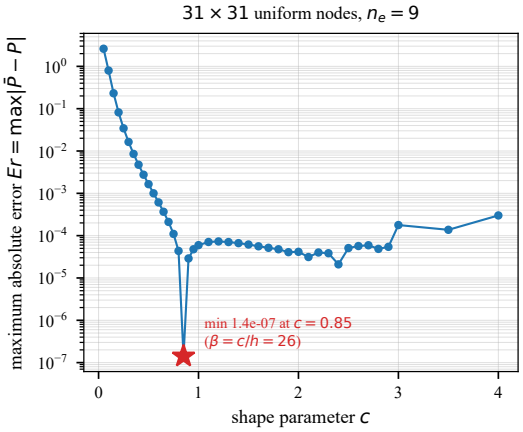

Figure 5. Maximum absolute error of the Poisson test problem (3.1) against the shape parameter c on 31×31 uniform nodes with $n_e = 9$. The horizontal axis is the shape parameter c of the main text, set in italic lower case. The curve falls steeply, has an isolated sampled minimum at $c = 0.85$, remains in a broader low-error band over $0.9 \le c \le 2.5$, and then degrades. The error axis is logarithmic.

From Figure 5: As c increases from near zero to 0.9, the maximum absolute error falls steeply from order one to 2.9×10^{-5} at $c = 0.9$; over $0.9 \le c \le 2.5$ it remains in a band between about 2×10^{-5}

and 8×10^{-5}; and beyond $c \approx 2.5$, it deteriorates gradually (on the strongly anisotropic grids of Table 2, the loss is abrupt: At $c = 5$, a local matrix is numerically singular). An isolated sampled minimum of 1.4×10^{-7} occurs at $c = 0.85$, but its narrowness was not tested under finer parameter sampling or perturbations, so it is not selected as a robust design point. For the 31×31 uniform distribution used in this test, whose minimum nodal spacing is $h = 1/30$, the interval $0.9 \le c \le 2.5$ is therefore the favourable tested range, and $c = 1.0$ is a reasonable default.

3.4. Nondimensionalisation of the shape parameter

The result just quoted must not be read as a universal recommendation because c carries the dimension of length: It enters the MQ kernel only through the ratio r/c, and r scales with the nodal spacing. Expressed nondimensionally, $0.9 \le c \le 2.5$ at $h = 1/30$ means $27 \le \beta \le 75$ with

$$\beta = c/h. \tag{3.3}$$

All subsequent structured thin-domain calculations specify their shape parameters through (3.3); the preceding unit-square diagnostics also report dimensional c values directly.

Figure 6 reports the relative L_∞ error of the manufactured steady problem

$$u(x, y) = \cos\frac{\pi x}{L_x}\cos\frac{\pi y}{L_y}, \qquad \nabla^2 u = -\pi^2\left(L_x^{-2} + L_y^{-2}\right)u, \tag{3.4}$$

posed on the thin domain of Section 4, that is, on $[0, L_x] \times [0, L_y]$ with $L_x = 0.1$ m (the wall thickness) and $L_y = 1$ m, with a Dirichlet condition on $x = 0$ and the direct-method Neumann treatment on the other three faces, so that exactly the same operators are exercised as in the transient example. Two features are relevant.

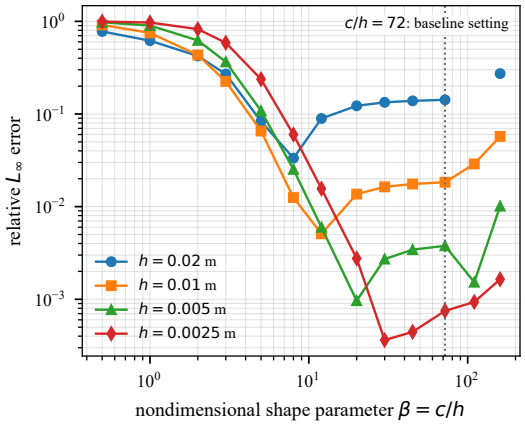

Figure 6. Relative L_∞ error of the manufactured problem (3.4) as a function of the nondimensional shape parameter $\beta = c/h$, for four nodal spacings, with $n_e = 9$. The dotted line marks $\beta = 72$. The optimum shifts to larger β as the grid is refined. Both axes are logarithmic.

First, the error is a non-monotone function of β with a pronounced minimum: For small β, the MQ kernel is too peaked to reproduce a smooth field, while for large β, the local matrix becomes so ill-conditioned that round-off dominates. This is the trade-off principle of Schaback [29].

Second, and more consequentially, *the minimum nodal spacing is not the nondimensionalising length that removes the mesh dependence*. Table 4 locates the optimum on four grids for four stencil sizes on a logarithmic grid of 22 values of β.

Table 4. Optimal shape parameter on the manufactured problem (3.4), located on a logarithmic grid of 22 values of β. $L_x = 0.1$ m is the wall thickness. Note that for $n_e = 9$, β^* varies by a factor of 4.6 across the grids, whereas c^*/L_x varies by a factor of 1.7; over the whole table, c^*/L_x stays within 0.82–1.72.

		$n_e = 5$		$n_e = 9$		$n_e = 13$		$n_e = 21$	
Nodes	h (m)	β^*	c^*/L_x	β^*	c^*/L_x	β^*	c^*/L_x	β^*	c^*/L_x
6	0.02	7.1	1.42	7.1	1.42	7.1	1.42	8.6	1.72
11	0.01	12.6	1.26	10.4	1.04	12.6	1.26	15.2	1.52
21	0.005	22.3	1.11	18.4	0.92	22.3	1.11	22.3	1.11
41	0.0025	39.5	0.99	32.6	0.82	47.8	1.20	32.6	0.82
fitted scaling $\beta^* \propto h^s$		$s = -0.83$		$s = -0.74$		$s = -0.91$		$s = -0.63$	

On this fixed domain, β^* is not constant: It grows as h^s with s between -0.63 and -0.91, so neither a fixed β nor a fixed c is shown to be universal. Because L_x is held fixed in the sweep, $c^*/L_x = O(1)$, ranging from 0.82 to 1.72 over the tested values of h and n_e. This observation suggests that the wall thickness is a relevant candidate scale for this benchmark, but it does not establish a transferable geometric scaling law; tests on geometrically rescaled domains would be needed for that conclusion.

This also clarifies the relationship to the criterion of Zheng et al. [30], in which c is selected through a test differential equation with a known solution. The present table supplies a benchmark calibration for the fixed domain and stencil families tested here. It should be used as a starting bracket followed by an error and conditioning check, not as a transferable rule. In these tests, cases with c/h near or above 100 can become numerically singular.

In the $n_e = 9$ manufactured-problem sweep of Table 4, $\beta = 72$ gives errors six to 20 times the best sampled values across the four listed grids. The single- and two-layer calculations nevertheless use $c = 0.6$ m and $c = 0.36$ m, respectively, and the five-layer calculations $c = 0.288$ m, all corresponding to the common convention $\beta = 72$. This convention is kept because, in the transient single-layer sweep of Section 4.5, $\beta = 72$ gives the smallest error among the usable $n_e = 9$ settings (Table 13).

3.5. Thin-walled convergence

For thin-walled structures, to ensure uniform node distribution, the number of points on the thin-walled side will be very small. To determine the minimum number of points, this section investigates the influence of different thin-walled-side point numbers on computational accuracy. The test problem is the steady Poisson problem on the thin rectangle $[0, 0.1] \times [0, 1]$—the geometry of Section 4—with Dirichlet data taken from the exact solution on all four faces. The long-edge direction is fixed at 121 points ($h = 1/120$), the thin-walled-side point number varies, and the shape parameter is $c = 0.60$, i.e., $\beta = c/h = 72$ on grids whose thin-side spacing is $1/120$ or coarser—the value used throughout Section 4—rising to $\beta = 120$ on the grid with 21 points across the thickness, with $n_e = 9$ and $n_b = 5$.

Three different analytical solution functions are considered: $u_1(x, y) = e^{x+y}$, $u_2(x, y) = x^2 + y^2$, and $u_3(x, y) = x^2y^3$. The corresponding maximum absolute errors are summarised in Table 5.

Table 5. Maximum absolute error against the thin-walled-side point number for three test solutions.

Thin-walled-side points	21	11	10	9	8	7	6	5
$u_1 = e^{x+y}$	6.5×10^{-7}	6.9×10^{-7}	7.6×10^{-7}	9.0×10^{-7}	1.1×10^{-6}	1.5×10^{-6}	2.1×10^{-6}	3.3×10^{-6}
$u_2 = x^2 + y^2$	5.7×10^{-7}	5.7×10^{-7}	6.2×10^{-7}	7.3×10^{-7}	8.8×10^{-7}	1.3×10^{-6}	1.8×10^{-6}	2.9×10^{-6}
$u_3 = x^2y^3$	6.8×10^{-8}	1.1×10^{-7}	1.7×10^{-7}	2.9×10^{-7}	4.5×10^{-7}	1.6×10^{-6}	2.3×10^{-6}	3.7×10^{-6}

Reducing the thin-side point count from 21 to five increases the maximum error in this test from 6.5×10^{-7} to 3.3×10^{-6} for u_1, while every entry remains below 4×10^{-6}. Across the three test functions, the listed errors lie between 10^{-8} and 4×10^{-6}. Thus, for this Poisson problem and the stated parameters, the five-point thin-side grid remains within the reported error range. The across-thickness node count and the one-dimensional boundary-stencil size n_b are distinct parameters; the effect of n_b is examined separately below.

The boundary stencil size n_b deserves a separate comment because it controls one source of negative boundary values observed in the present scheme. Table 6 lists the temperature computed at the adiabatic face $x = L_x$ of the single-layer example at $t = 200$ s for four values of n_b at three values of β; the exact value is 5.92×10^{-13} °C. For $\beta = 12$ and 20, the undershoot magnitude grows by more than three orders of magnitude between $n_b = 3$ and $n_b = 9$. At $\beta = 72$, the boundary artefact changes sign at $n_b = 7$, while the global L_∞ error degrades by a factor of about six only at $n_b = 9$. Thus a large boundary stencil can eventually affect the global error; for $n_b \leq 5$, the effect remains a localized artefact of the one-dimensional derivative stencil and the listed global error norm is unchanged to the shown precision. We use $n_b = 3$ throughout Section 4.

Table 6. Temperature at the adiabatic face at $t = 200$ s (exact value 5.92×10^{-13} °C) as a function of the boundary stencil size n_b; single-layer example, 11 nodes across the thickness.

β	$n_b = 3$	$n_b = 5$	$n_b = 7$	$n_b = 9$
12	-2.88×10^{-5}	-8.52×10^{-4}	-1.76×10^{-2}	-1.28×10^{-1}
20	-2.85×10^{-5}	-8.36×10^{-4}	-1.65×10^{-2}	-7.86×10^{-2}
72	-2.83×10^{-5}	-8.15×10^{-4}	$+4.40 \times 10^{-2}$	$+9.15$

4. Multilayer heat-conduction simulations

This section employs LRBFCM to simulate heat conduction in single-layer, two-layer, and five-layer thin-walled media. The method is first verified against an exact solution (Section 4.3) and then compared with the finite element formulations under the conditions reported in Section 4.4.

Coordinate convention. Throughout Section 4, x is the *through-thickness* coordinate, along which the layers are stacked, and y is the *along-length* coordinate. The thin-walled body therefore occupies $0 \leq x \leq 0.1$ m and $0 \leq y \leq 1$ m. Node counts are quoted as (number across the thickness) × (number along the length).

The two-dimensional heat conduction equation without heat source is

$$\frac{\partial u(x,y,t)}{\partial t} = \alpha \nabla^2 u(x,y,t), \quad (x,y) \in \Omega, \quad t > 0, \tag{4.1}$$

where α is the thermal diffusivity in units of m^2/s, calculated by the following equation:

$$\alpha = \frac{k}{\rho c_p}, \tag{4.2}$$

where k is the thermal conductivity, ρ is the material density, and c_p is the specific heat capacity.

4.1. Assembly of the discrete system

Let N be the total number of collocation nodes. The nodes are partitioned into four disjoint sets: interior nodes $\mathcal{I}$, Dirichlet boundary nodes $\mathcal{D}$, Neumann boundary nodes $\mathcal{N}$, and interface nodes $\mathcal{S}$ lying on a material discontinuity. Corner nodes at which two boundary conditions meet are assigned to the face carrying the driving condition, so that each node contributes exactly one row.

Three global arrays are assembled, all of size $N \times N$ except the last: $\mathbf{A}$, $\mathbf{H}$, and $\mathbf{b} \in \mathbb{R}^N$. Row i of each is built as follows.

Interior node $i \in \mathcal{I}$. The stencil is the set of the n_e nodes nearest to $\mathbf{x}_i$ in the Euclidean sense, including $\mathbf{x}_i$ itself, obtained from a k-d tree search. With $\mathbf{\Phi}_{n_e \times n_e}$ denoting the local MQ matrix of that stencil and $\nabla^2 \mathbf{\Theta}_{n_e}$ the row vector of Laplacians (2.9) evaluated at $\mathbf{x}_i$,

$$\mathbf{A}_{i,\,\mathrm{stencil}(i)} = \alpha_i \, \nabla^2 \mathbf{\Theta}_{n_e}(\mathbf{x}_i) \, \mathbf{\Phi}^{-1}_{n_e \times n_e}, \qquad \mathbf{H}_{ii} = 1, \qquad b_i = 0, \tag{4.3}$$

where α_i is the thermal diffusivity of the layer containing $\mathbf{x}_i$. All remaining entries of the row are zero.

Dirichlet node $i \in \mathcal{D}$. Since $\mathbf{\Theta}_{n_e}(\mathbf{x}_i)\mathbf{\Phi}^{-1}_{n_e \times n_e} = \mathbf{e}_i$ exactly, the row reduces to

$$\mathbf{A}_{ii} = 1, \qquad \mathbf{H}_{ii} = 0, \qquad b_i = p_D(\mathbf{x}_i). \tag{4.4}$$

Neumann node $i \in \mathcal{N}$. The direct method of Zheng et al. [25] is used: The stencil is reduced to the n_b nodes lying on the grid line normal to the boundary and marching inward, so that the normal derivative is evaluated from a one-dimensional interpolation. Define the signed outward-normal coordinate at node i by $q_i(\mathbf{x}) = \mathbf{n}_i \cdot (\mathbf{x} - \mathbf{x}_i)$, so $q_i = 0$ at the boundary node and the inward stencil nodes have $q_i \le 0$. With $\mathbf{\Phi}_{n_b \times n_b}$ denoting the corresponding one-dimensional MQ matrix,

$$\mathbf{A}_{i,\,\mathrm{stencil}(i)} = \frac{\partial \mathbf{\Theta}_{n_b}}{\partial q_i}(0) \, \mathbf{\Phi}^{-1}_{n_b \times n_b}, \qquad \mathbf{H}_{ii} = 0, \qquad b_i = p_N(\mathbf{x}_i). \tag{4.5}$$

Eq (4.5) therefore evaluates $\partial u/\partial n = \mathbf{n}_i \cdot \nabla u$ with the outward normal on every face, including the inhomogeneous test in Section 3.2.

Interface node $i \in \mathcal{S}$. Temperature continuity is automatic because a single node is shared by the two layers. Let the common coordinate s increase from the minus layer to the plus layer (here, $s = x$). Heat-flux continuity, $k^- \partial u^-/\partial s = k^+ \partial u^+/\partial s$, is imposed by forming two one-sided derivative rows with respect to that same coordinate, drawing the nodes for each row from its own layer, and taking their conductivity-weighted difference:

$$\mathbf{A}_{i,\cdot} = k^- \frac{\partial \mathbf{\Theta}^-_{n_b}}{\partial s}(\mathbf{\Phi}^-)^{-1} - k^+ \frac{\partial \mathbf{\Theta}^+_{n_b}}{\partial s}(\mathbf{\Phi}^+)^{-1}, \qquad \mathbf{H}_{ii} = 0, \qquad b_i = 0. \tag{4.6}$$

With this partition, $\mathbf{H} = \mathrm{diag}(\eta_i)$ with $\eta_i = 1$ for $i \in \mathcal{I}$ and $\eta_i = 0$ otherwise, so $\mathbf{H}$ is singular; the rows it annihilates are exactly the rows in which $\mathbf{A}$ carries an algebraic constraint rather than a time-evolution equation. The semi-discrete system is therefore the differential-algebraic system

$$\mathbf{H}\dot{\mathbf{u}} = \mathbf{A}\mathbf{u} - \mathbf{b}. \tag{4.7}$$

Applying the backward Euler scheme to (4.7) gives

$$\frac{\mathbf{H}(\mathbf{u}^{n+1} - \mathbf{u}^n)}{\Delta t} = \mathbf{A}\mathbf{u}^{n+1} - \mathbf{b}, \tag{4.8}$$

and hence the time-marching form that is actually solved,

$$(\mathbf{H} - \Delta t\, \mathbf{A})\mathbf{u}^{n+1} = \mathbf{H}\mathbf{u}^n - \Delta t\, \mathbf{b}, \tag{4.9}$$

where n is the time-step index and Δt the time step. The load vector $\mathbf{b}$ is essential and must not be omitted. For $i \in \mathcal{D}$, the ith row of (4.9) reads $-\Delta t\, u_i^{n+1} = -\Delta t\, b_i$, that is, $u_i^{n+1} = p_D(\mathbf{x}_i)$, whereas dropping $\mathbf{b}$ would enforce $u_i^{n+1} = 0$ and the inhomogeneous Dirichlet condition would never enter the calculation. Since $\mathbf{H}$, $\mathbf{A}$, and Δt are all constant in time, $\mathbf{H} - \Delta t\mathbf{A}$ is factorized once by a sparse lower-upper (LU) decomposition, and only a triangular solve is performed per step. The initial condition is $u_i^0 = u_{\mathrm{init}}(\mathbf{x}_i)$ at every node; the boundary data are applied as a step change from the first step onward, consistent with the benchmark solution of Section 4.3.

Algorithm 1 summarises the procedure.

Algorithm 1 assembly and solution.

1. Generate the node set; record the minimum nodal spacing $h = \min_i \min_{j \neq i} \|\mathbf{x}_i - \mathbf{x}_j\|$.
2. Set the shape parameter from the nondimensional rule $c = \beta h$ (Section 3.4).
3. Build a k-d tree over the node set.
4. For each node, classify it as interior, Dirichlet, Neumann, or interface and build its row by (4.3), (4.4), (4.5), or (4.6); assemble into sparse $\mathbf{A}$, diagonal $\mathbf{H}$, and vector $\mathbf{b}$.
5. Factorize $\mathbf{H} - \Delta t\mathbf{A}$ once.
6. March (4.9) to the required time, reusing the factorization.

4.2. Single-layer thin-walled heat conduction

Consider a concrete thin-walled body of thickness 0.1 m (x direction) and length 1 m (y direction). Material parameters: density $\rho = 2300$ kg/m^3, thermal conductivity $k = 0.72$ W/(m $\cdot^\circ$ C), and specific heat capacity $c_p = 780$ J/(kg $\cdot^\circ$ C). The thermal diffusivity follows from these as $\alpha = k/(\rho c_p)$=4.013378×10^{-7}m^2/s. The value is quoted to seven digits because rounding it to three digits displaces the temperature at $t = 5000$ s by up to 0.03 °C—larger than the discretization error of the converged solutions reported below. Accordingly, α is computed from k, ρ, and c_p throughout. $\Gamma_1 = \{x = 0\}$, $\Gamma_2 = \{y = L_y\}$, $\Gamma_3 = \{y = 0\}$, and $\Gamma_4 = \{x = L_x\}$ label the four physical faces; these face labels are independent of the boundary-type symbols Γ_D and Γ_N in Section 2. Figure 7 shows the geometry, the boundary conditions, and the node distribution.

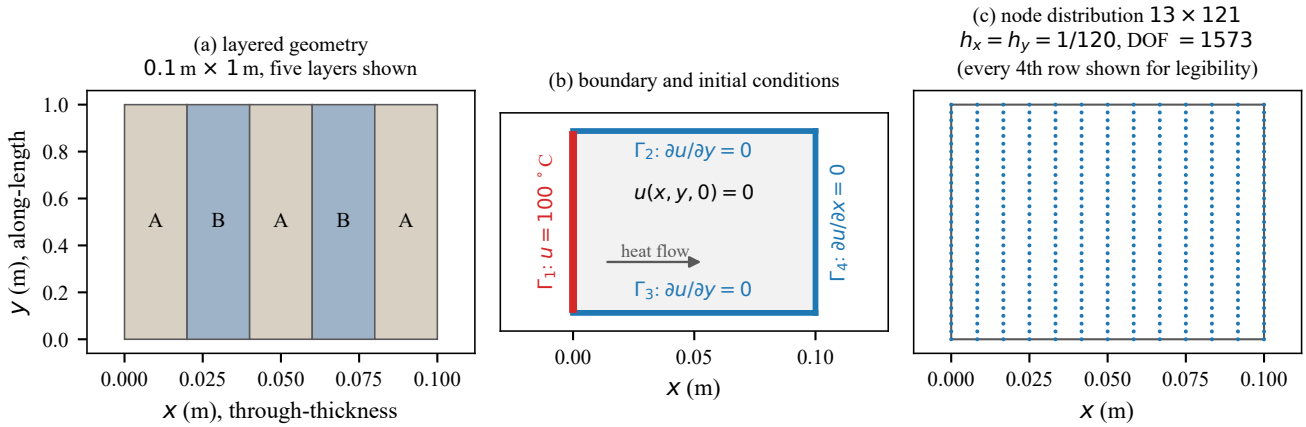

Figure 7. Thin-walled model, boundary conditions, and node distribution. Panel (a) shows the layer stacking for the five-layer case; the single- and two-layer cases use the same outline. Panel (b) states the conditions (4.10)–(4.13). Panel (c) shows the node distribution of the single-layer example.

Boundary conditions are shown in Figure 7(b). The left boundary Γ_1 temperature is fixed at 100 °C:

$$u(x, y, t) = 100, \quad (x, y) \in \Gamma_1, \quad t > 0. \tag{4.10}$$

Top and bottom boundaries Γ_2, Γ_3 are adiabatic:

$$\frac{\partial u(x, y, t)}{\partial y} = 0, \quad (x, y) \in \Gamma_2 \cup \Gamma_3, \quad t > 0. \tag{4.11}$$

Right boundary Γ_4 is adiabatic:

$$\frac{\partial u(x, y, t)}{\partial x} = 0, \quad (x, y) \in \Gamma_4, \quad t > 0. \tag{4.12}$$

Initial condition:

$$u(x, y, 0) = 0. \tag{4.13}$$

The baseline settings for the single- and multilayer simulations of this section are collected in Table 7; the validation, parameter-sweep, and finite element method (FEM) studies state their distinct settings locally.

Table 7. Baseline computational settings for the single- and multilayer simulations. n_e is the two-dimensional interior stencil, n_b the one-dimensional boundary and interface stencil, h the nodal spacing (equal in both directions), $\beta = c/h$ the nondimensional shape parameter, and DOF denotes degrees of freedom.

Example	Nodes ($x \times y$)	DOF	h (m)	β	c (m)	n_e	n_b	Δt (s)
Single layer	13×121	1573	1/120	72	0.6	9	3	see below
Two layers	21×201	4221	0.005	72	0.36	9	3	see below
Five layers	26×251	6526	0.004	72	0.288	9	3	see below

Each reported target-time field is computed independently from the zero field at $t = 0$ with one constant step: $\Delta t = 10^{-3}$ s for targets $t \le 1$ s, 0.5 s for the target $t = 200$ s, 1 s for targets through $t = 1000$ s, 2 s for targets through $t = 5000$ s, and 5 s for later targets through $t = 10000$ s. These are target-time rules, not consecutive stages of one continued trajectory. Extrapolating the first-order rate of Table 8 to $\Delta t = 2$ s gives, at $t = 5000$ s, a temporal error of about 4×10^{-5} relative, below the spatial error of every grid in Table 9 except the finest, which is not used in the examples of this section. The five monitoring points $(x, y) = (0.02, 0.5)$, $(0.04, 0.5)$, $(0.06, 0.5)$, $(0.08, 0.5)$, $(0.10, 0.5)$ span the thickness at the mid-length section. On the 13×121 grid, the nodal abscissae in the thickness direction are multiples of $1/120$, so four of these five points are not nodes, and at very small times, the field is unresolved there (at $t = 1$ s, the thermal penetration depth $\sqrt{\alpha t} = 6.3 \times 10^{-4}$ m is only $0.076h$), so a value interpolated at such a point reflects the interpolation stencil rather than the temperature field. All values quoted below are therefore nodal values. The exact-solution accuracy comparisons are made at $t = 5000$ s, where the field is resolved; the $t = 200$ s profiles are shown as descriptive early-time results.

Table 8. Temporal convergence at $t = 5000$ s, 16441 DOF.

Δt (s)	steps	$\|u - u_{\text{ref}}\|_\infty/100$	observed rate
100	50	2.09×10^{-3}	—
50	100	1.03×10^{-3}	1.01
25	200	5.11×10^{-4}	1.02
12.5	400	2.51×10^{-4}	1.03
6.25	800	1.21×10^{-4}	1.05
3.125	1600	5.66×10^{-5}	1.10

Table 9. Verification of LRBFCM against the exact solution (4.14). Panel (a) uses the 1573-DOF baseline grid ($h = 1/120$ m, $\beta = 72$, $n_e = 9$, and $n_b = 3$); panel (b) uses $\Delta t = 2$ s, $\beta = 72$, $n_e = 9$, $n_b = 3$. The L_∞ errors are normalized by $\max|u| = 100\,^\circ$C and the L_2 errors by the root mean square of the exact solution; the observed rate is computed from the L_∞ column.

(a) Baseline-grid errors at several independently computed target times

t (s)	Δt (s)	steps	relative L_2 error	relative L_∞ error
200	0.5	400	1.36×10^{-2}	1.11×10^{-2}
1000	1	1000	3.25×10^{-3}	2.32×10^{-3}
5000	2	2500	3.67×10^{-4}	4.27×10^{-4}
10000	5	2000	1.40×10^{-4}	1.39×10^{-4}

(b) Spatial convergence at $t = 5000$ s

DOF	h (m)	relative L_2 error	relative L_∞ error	observed rate
306	0.02	2.14×10^{-3}	1.98×10^{-3}	—
1111	0.01	4.28×10^{-4}	4.92×10^{-4}	2.01
4221	0.005	1.92×10^{-4}	2.16×10^{-4}	1.19
16441	0.0025	7.14×10^{-5}	7.97×10^{-5}	1.44
64881	0.00125	3.26×10^{-5}	3.02×10^{-5}	1.40

4.3. *Verification against the exact solution*

Because the faces $y = 0$ and $y = L_y$ are adiabatic and the initial state is uniform, the single-layer problem (4.10)–(4.13) has no y-dependence and admits the classical closed-form solution of a slab with a step surface temperature $u_b = 100\,^{\circ}\mathrm{C}$ and an insulated rear face

$$u(x,t) = u_b\left[1 - \frac{4}{\pi}\sum_{n=0}^{\infty}\frac{1}{2n+1}\sin(\lambda_n x)\exp(-\alpha\lambda_n^2 t)\right], \qquad \lambda_n = \frac{(2n+1)\pi}{2L_x}. \tag{4.14}$$

For $\sqrt{\alpha t} \ll L_x$, the eigenfunction series suffers cancellation. We then evaluate the mathematically equivalent reflected-image series

$$u(x,t) = u_b\sum_{m=0}^{\infty}(-1)^m\left[\operatorname{erfc}\left(\frac{2mL_x + x}{2\sqrt{\alpha t}}\right) + \operatorname{erfc}\left(\frac{2(m+1)L_x - x}{2\sqrt{\alpha t}}\right)\right]. \tag{4.15}$$

The reflected term enforces insulation at $x = L_x$; the implementation switches between the two exact series in their numerically stable ranges. Eq (4.14) was checked independently against a one-dimensional implicit finite-difference solution on 4001 nodes, Richardson extrapolated in Δt, which reproduces it to $4.6 \times 10^{-7}\,^{\circ}\mathrm{C}$. At $t = 5000$ s and the same $\Delta t = 2$ s, the finest PLANE77 result (48,881 nodes) differs from the 4001-node finite-difference result by at most $1.4 \times 10^{-6}\,^{\circ}\mathrm{C}$ over the five monitoring positions.

Table 9(a) reports relative L_2 and L_∞ errors of the baseline grid with 1573 degrees of freedom (DOF) against (4.14) at four target times. Each target is computed independently from the zero field with the constant time step listed in the table. This explicitly quantifies the larger early-time error without using that under-resolved result to support an accuracy or efficiency conclusion. Table 9(b) and Figure 8(a) report the same norms under h-refinement at $t = 5000$ s with $\beta = 72$ held fixed. The observed rate is 2.0 on the first refinement and falls to about 1.2–1.4 on the finer grids. Two effects contribute to the degradation: The temporal error of the fixed step $\Delta t = 2$ s becomes comparable to the spatial error from the 16441-DOF grid onward (Table 8), and holding β fixed under refinement incurs the conditioning penalty anticipated in Section 3.4.

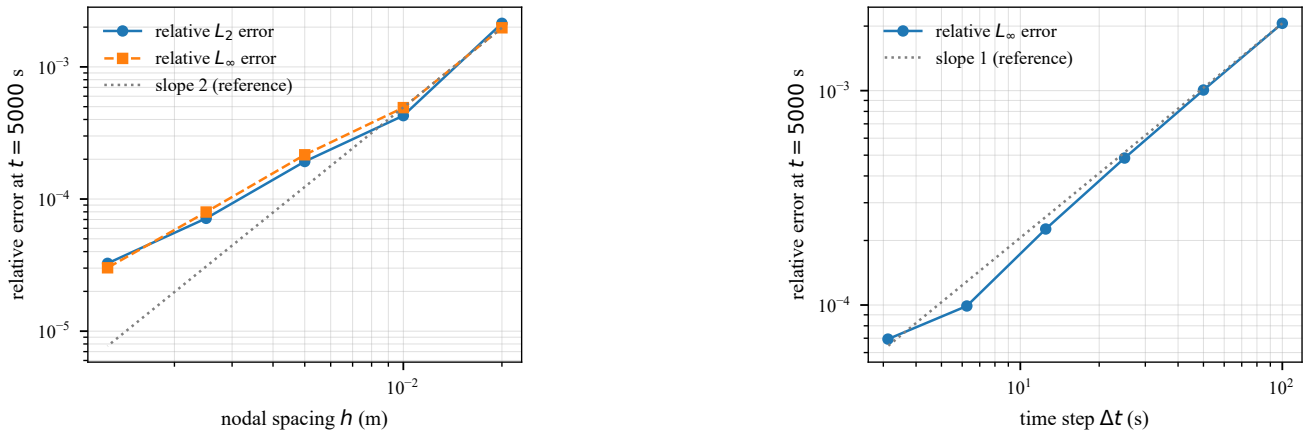

(a) spatial refinement, $\Delta t = 2$ s

(b) temporal refinement, 16441 DOF

Figure 8. Convergence of LRBFCM against the exact solution (4.14) at $t = 5000$ s. The L_∞ errors are normalized by $\max|u| = 100\,^{\circ}\mathrm{C}$ and the L_2 errors by the root mean square of the exact solution. Both panels use logarithmic axes.

Table 8 and Figure 8(b) report temporal refinement on a fixed grid. The observed rate is 1.0, as expected of the backward Euler scheme (4.9). Table 8 measures the errors against a reference solution obtained with $\Delta t = 0.390625$ s (12800 steps), so as to remove the spatial error floor and isolate the temporal term; Figure 8b shows the same refinement measured against the exact solution (4.14), where the 8×10^{-5} spatial floor becomes visible at the smallest steps.

As a separate check of the interface rows in (4.6), the converged steady solution is compared with the analytical series-resistance profile. For a layered slab held at u_b on one face and at zero on the other, the steady heat flux is $q = u_b / \sum_i d_i/k_i$, with the temperature at each interface following by accumulation. This analytical reference is independent of the LRBFCM discretization, but the comparison checks steady interface assembly rather than transient multilayer accuracy. Table 10 shows that the LRBFCM reproduces this profile to better than 5×10^{-3} °C, the largest error occurring for the five-layer concrete/steel stack (conductivity ratio 84); the glass/air stack, ratio 53.8, is reproduced to 1.4×10^{-3} °C.

Table 10. Maximum nodal error of the steady layered solution against the exact series-resistance profile.

Configuration	DOF	Conductivity ratio	Max nodal error (°C)
Two layers, concrete/steel	4221	84.0	2.47×10^{-5}
Five layers, concrete/steel	6526	84.0	4.70×10^{-3}
Five layers, glass/air	6526	53.8	1.43×10^{-3}

4.4. Comparison with the finite element method

4.4.1. The negative temperatures at small time

At small times, the computed minimum temperature depends strongly on the finite element formulation. The controlled runs below associate the observed undershoot with the particular formulation and element order tested.

The run settings are collected in Table 11. All of those calculations used ANSYS Mechanical APDL 2025 R2 (Build 25.2, UP20250519), a mapped quadrilateral mesh on the same geometry, the full transient solver with $\Delta t = 10^{-3}$ s, and the same material data. Element type, time-integration parameter, capacitance lumping, and mesh density were varied as listed. All reported MAPDL runs completed successfully under the stated settings. The APDL does not override `EQSLV` or `CNVTOL`; MAPDL defaults therefore apply.

With eight-node quadratic elements, the minimum is -14.590 °C at 10061 nodes and -14.425 °C at 39453 nodes. This is not round-off. For a field whose scale is 100 °C, the double-precision resolution is $100\varepsilon = 2.2 \times 10^{-14}$; the observed undershoot is 6.6×10^{14} times that floor. The much smaller entries retained in the table document their signs but are treated as zero within the stated numerical precision. In these tests, the large negative value occurs with the eight-node quadratic element and not with the four-node linear element. Changing θ or the ANSYS lumped-capacitance switch (LUMPM) in the listed cases does not remove it; row-sum lumping of this quadratic element retains negative corner entries.

Prior finite element analysis has documented that small time steps combined with consistent-mass formulations can violate discrete maximum-principle behaviour [31]. This provides qualitative

background for the present observation, but no mesh-dependent critical threshold is inferred for the two-dimensional PLANE77 calculation. At the listed early instant, the tested quadratic-element formulation produces a substantial undershoot. In a separate LRBFCM run on 4221 nodes, every one of the 1000 steps from $t = 10^{-3}$ to 1 s was inspected; no negative value above the double-precision floor was observed for $n_e = 9$ and $\beta = 72$. This finite test does not establish an unconditional time-step restriction or a general discrete maximum principle for the LRBFCM. Figure 9 summarises the comparison.

Table 11. Minimum temperature at $t = 5 \times 10^{-3}$ s and $\Delta t = 10^{-3}$ s. θ is the first-order time-integration parameter; LUMPM is the ANSYS lumped-capacitance switch.

Element	Order	Nodes	θ	LUMPM	Minimum temperature (°C)
PLANE55	4-node linear	13283	1.0	off	$+1.10 \times 10^{-147}$
PLANE55	4-node linear	13283	1.0	on	$+1.10 \times 10^{-147}$
PLANE55	4-node linear	13283	0.5	off	$+2.08 \times 10^{-157}$
PLANE55	4-node linear	4221	1.0	off	$+2.74 \times 10^{-90}$
PLANE77	8-node quadratic	10061	1.0	off	**−14.590**
PLANE77	8-node quadratic	10061	1.0	on	−14.590
PLANE77	8-node quadratic	10061	0.5	off	−14.595
PLANE77	8-node quadratic	39453	1.0	off	−14.425

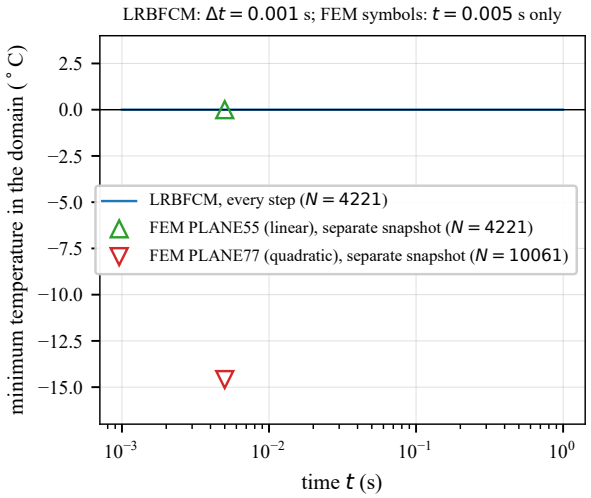

Figure 9. Minimum nodal temperature in the domain. The LRBFCM curve records every accepted step from $t = 10^{-3}$ to 1 s (4221 DOF, $\Delta t = 10^{-3}$ s, $n_e = 9, \beta = 72$). The two FEM symbols are separate MAPDL snapshots at $t = 5 \times 10^{-3}$ s and $\Delta t = 10^{-3}$ s: PLANE55 on 4221 nodes and PLANE77 on 10061 nodes. They are not time-history minima.

4.4.2. Error, degrees of freedom, and reported solve time

Table 12 reports the results at $t = 5000$ s against benchmark (4.14), using the error measure and time-step conditions stated in its caption. The runs used Windows 11 Pro on an AMD Ryzen 9 5900X with 32 GB RAM; MAPDL was launched with four processes. No common peak-memory measurement was made for both implementations. Error and degrees of freedom are reported

together; the timings are descriptive because the implementations and solver workflows differ.

Table 12. Accuracy and cost at $t = 5000$ s and $\Delta t = 2$ s. The error is the maximum over the five monitoring points, measured against (4.14).

Method	DOF	Max error (°C)	Solve time (s)	Implementation
LRBFCM	306	1.98×10^{-1}	0.1	Python/SciPy
LRBFCM	1111	4.92×10^{-2}	0.1	Python/SciPy
LRBFCM	4221	2.16×10^{-2}	0.5	Python/SciPy
LRBFCM	16441	7.97×10^{-3}	2.6	Python/SciPy
FEM, 4-node linear	306	4.59×10^{-1}	10	ANSYS APDL
FEM, 4-node linear	1111	1.11×10^{-1}	12	ANSYS APDL
FEM, 4-node linear	4221	2.62×10^{-2}	23	ANSYS APDL
FEM, 4-node linear	16441	5.16×10^{-3}	77	ANSYS APDL
FEM, 8-node quadratic	861	4.72×10^{-3}	12	ANSYS APDL
FEM, 8-node quadratic	3221	4.08×10^{-3}	18	ANSYS APDL
FEM, 8-node quadratic	12441	4.10×10^{-3}	55	ANSYS APDL

The table provides discrete samples rather than matched-accuracy mesh pairs, so no degree-of-freedom ratio is inferred between the LRBFCM and four-node linear elements. Against eight-node quadratic elements, the tested LRBFCM formulation has no accuracy-per-degree-of-freedom advantage: The quadratic formulation reaches 4.7×10^{-3} °C with 861 unknowns. The two finer PLANE77 rows cluster near 4.1×10^{-3} °C, while the finest listed LRBFCM and PLANE55 errors are 7.97×10^{-3} and 5.16×10^{-3} °C, respectively. Because the fixed $\Delta t = 2$ s contributes temporal error to the finest entries, these rows are not a pure spatial comparison. Section 4.5 therefore uses $\Delta t = 0.25$ s for the LRBFCM accuracy sweep and lists the matching-step FEM accuracy runs separately.

The solve times in Table 12 are reported for completeness but do not support a conclusion about the methods because the implementations and solver workflows differ.

Figure 10 plots the maximum error against the degrees of freedom from Table 12.

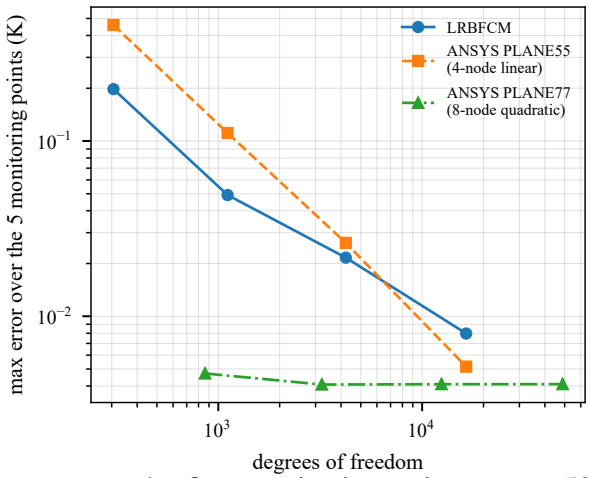

Figure 10. Maximum error over the five monitoring points at $t = 5000$ s against Eq (4.14), plotted against the number of degrees of freedom; $\Delta t = 2$ s.

4.5. Later-time accuracy and early-time undershoot

The calibration and early-time results motivate examining later-time error and negative excursion together. These quantities require different time resolutions, so they were not extracted from one time-marching history. For each LRBFCM setting in Table 13, two independent simulations start from the zero initial field at $t = 0$: (i) an accuracy run uses constant $\Delta t = 0.25$ s to the target time $t = 5000$ s, and (ii) an early-time run uses constant $\Delta t = 10^{-3}$ s and inspects the minimum nodal temperature after every one of the 1000 accepted steps through $t = 1$ s. No state is passed between the two runs.

Table 13. LRBFCM sweep on 4221 nodes with $n_b = 3$. The error is the maximum absolute error over the five monitoring points against (4.14) at $t = 5000$ s with constant $\Delta t = 0.25$ s; the early minimum is inspected after every step through $t = 1$ s with constant $\Delta t = 10^{-3}$ s in an independent run. "No obs". means $\min u \geq -100\varepsilon = -2.2\times10^{-14}$ °C; it is an observation over this finite window, not a monotonicity proof. "Unusable" denotes a finite but nonphysical accuracy field, and — denotes failed assembly.

	$n_e = 9$ (3×3 stencil)			$n_e = 13$		
β	Error (K)	Early min u (°C)	Status	Error (K)	Early min u (°C)	Status
10	9.854×10^{-2}	-3.272×10^{-47}	no obs.	2.332×10^{-2}	-1.305×10^{-1}	observed
15	7.819×10^{-2}	-3.067×10^{-47}	no obs.	1.390×10^{-2}	-1.226×10^{-1}	observed
22.28	5.094×10^{-2}	-2.995×10^{-47}	no obs.	5.516×10^{-3}	-1.191×10^{-1}	observed
33	3.485×10^{-2}	-2.965×10^{-47}	no obs.	$\mathbf{2.065 \times 10^{-3}}$	-1.175×10^{-1}	observed
48	2.692×10^{-2}	-2.961×10^{-47}	no obs.	unusable	-1.166×10^{-1}	observed
72	$\mathbf{2.321 \times 10^{-2}}$	-2.981×10^{-47}	no obs.	4.049×10^{-3}	-1.212×10^{-1}	observed
110	2.355×10^{-2}	-2.946×10^{-47}	no obs.	3.696×10^{-2}	-3.768×10^{-1}	observed
160	unusable	-2.950×10^{-47}	no obs.	—	—	failed

For the usable $n_e = 9$ cases with $10 \leq \beta \leq 110$, no negative value above the double-precision floor is recorded over $t \leq 1$ s. Each usable $n_e = 13$ case in the same range has a negative excursion between 0.12 and 0.38 °C. At $n_e = 13, \beta = 48$, the early run remains finite, but the later accuracy run develops a nonphysical field; at $\beta = 160$, the $n_e = 9$ accuracy field is also unusable, and the $n_e = 13$ assembly fails. Thus, within this finite sweep, stencil size is associated with the observed early-excursion classification, while the shape parameter remains consequential for accuracy and numerical usability.

One possible explanation is the sign structure of the local discrete operator. Enlarging the stencil changes both the support and the weights of the local Laplacian. The present data do not isolate that mechanism, however, and no matrix-monotonicity theorem is claimed.

Table 14 selects two representative LRBFCM operating points from the usable paired rows reported in Table 13.

The FEM records cannot be added as paired rows to Table 14. Their later-time accuracy and early-time data come from different calculations, and the early records are single snapshots rather than minima over all steps. Table 15 therefore lists them as separate references without constructing synthetic accuracy-undershoot coordinates.

Even where the PLANE55 node count happens to match between the two runs, the early record covers only one instant and therefore cannot supply the every-step metric used for the LRBFCM. The PLANE77 accuracy and snapshot runs also use different meshes. These limits preclude a point-by-

point method-family ranking on a common accuracy-undershoot plane.

Table 14. Selected paired LRBFCM operating points. The later-time error is the maximum absolute error over the five monitoring points against (4.14); it and the early minimum come from the two independent constant-step protocols stated above. The first row has the smallest error among usable $n_e = 9$ cases with no observed undershoot; the second has the smallest error among the usable $n_e = 13$ cases with an observed undershoot.

Setting	DOF	Error (K)	Early min u (°C)	Classification
LRBFCM, $n_e = 9, \beta = 72$	4221	2.321×10^{-2}	-2.981×10^{-47}	no undershoot observed
LRBFCM, $n_e = 13, \beta = 33$	4221	2.065×10^{-3}	-1.175×10^{-1}	undershoot observed

Table 15. Separate MAPDL reference records. Accuracy rows and early snapshot rows are not paired; no row combines them into a common operating point.

Record	Formulation	Nodes	Protocol	Value
accuracy error	PLANE55	4221	$t = 5000$ s, $\Delta t = 0.25$ s	2.782×10^{-2} K
accuracy error	PLANE77	3221	$t = 5000$ s, $\Delta t = 0.25$ s	5.148×10^{-4} K
accuracy error	PLANE77	12441	$t = 5000$ s, $\Delta t = 0.25$ s	5.109×10^{-4} K
spatial minimum in one snapshot	PLANE55	4221	$t = 0.005$ s, $\Delta t = 0.001$ s	$+2.745 \times 10^{-90}$ °C
spatial minimum in one snapshot	PLANE77	10061	$t = 0.005$ s, $\Delta t = 0.001$ s	-14.590 °C

Figure 11 plots only the LRBFCM settings with valid paired metrics. The text box reproduces the unpaired FEM run values for context.

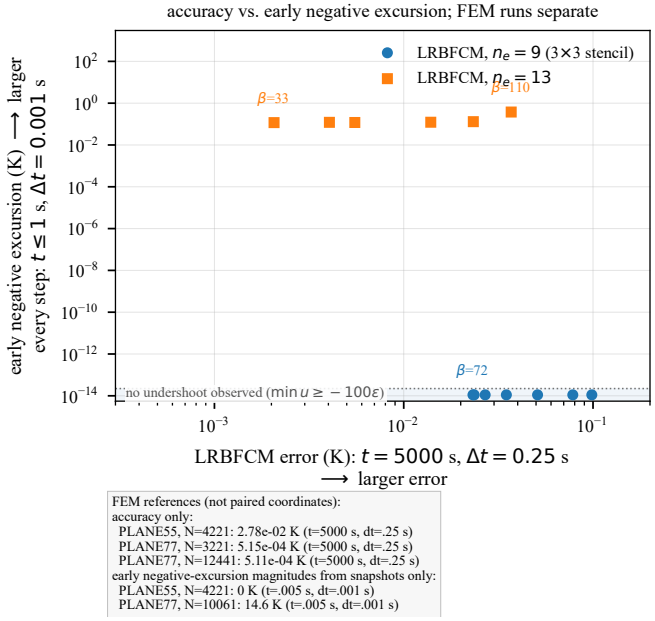

Figure 11. Later-time error against early negative excursion for the LRBFCM on 4221 nodes. Every plotted coordinate combines the two independent protocols stated above: maximum absolute error over the five monitoring points against (4.14) at $t = 5000$ s with $\Delta t = 0.25$ s and the minimum over all 1000 steps through $t = 1$ s with $\Delta t = 0.001$ s. The shaded floor denotes "no undershoot observed". FEM reference values are listed as unpaired text only and are not plotted as coordinates.

Figure 12 presents the through-thickness temperature profiles of the single-layer example, and Figure 13 documents, for every configuration of this section that the computed fields are one-dimensional in x.

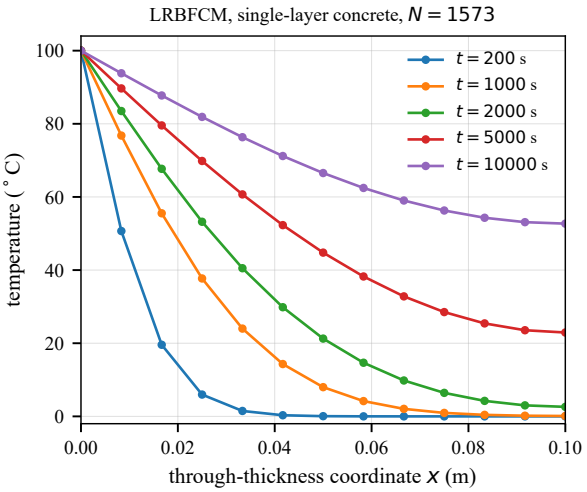

Figure 12. Through-thickness temperature profiles of the single-layer concrete wall at the mid-length section $y = 0.5$ m, at $t = 200$, 1000, 2000, 5000, and 10000 s (LRBFCM, 1573 DOF). Temperatures are in °C.

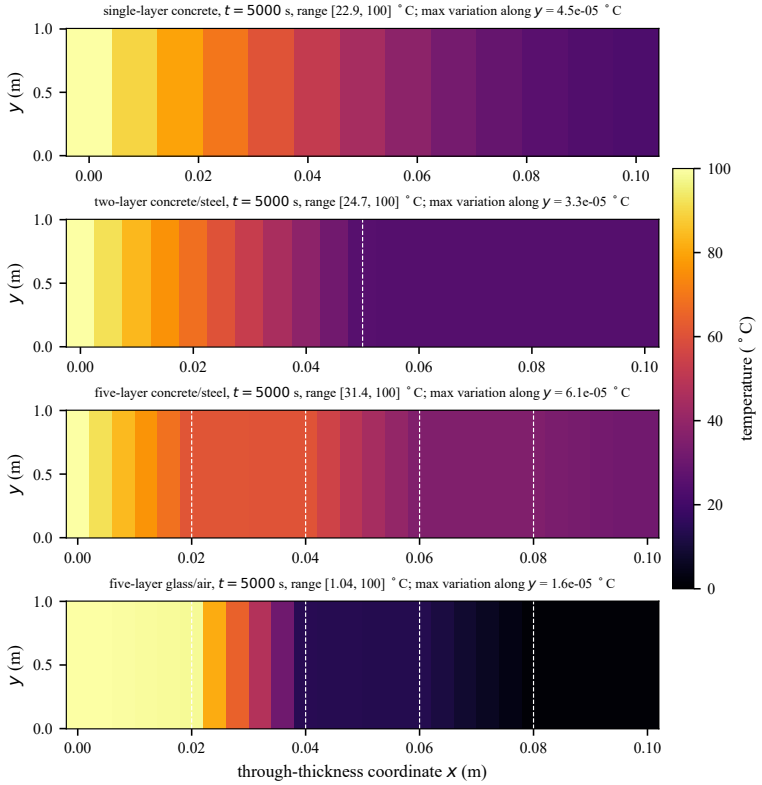

Figure 13. Temperature fields at $t = 5000$ s for all four configurations of this section, in °C over the range $[0, 100]$. Broken lines mark the material interfaces. The maximum variation along y is below 10^{-4} °C in every case, confirming that the solutions are one-dimensional in x; the through-thickness profiles of Figures 12 and 14–16 therefore carry the complete information.

4.6. Two-layer composite-wall heat conduction

The double-layer composite material consists of Material A (0.05 m thick × 1 m long, concrete, parameters as in Section 4.2) and Material B (0.05 m thick × 1 m long, structural steel), where structural steel has density $\rho_2 = 7850$ kg/m^3, thermal conductivity $k_2 = 60.5$ W/(m $\cdot^\circ$ C), specific heat capacity $c_{p2} = 434$ J/(kg $\cdot^\circ$ C), and thermal diffusivity $\alpha_2 = 1.78 \times 10^{-5}$ m^2/s. The two materials are tightly connected, forming a composite wall 0.1 m thick and 1 m long.

The heat conduction equations for the two materials are

$$\frac{\partial u_A}{\partial t} = \alpha_1 \nabla^2 u_A, \quad (x, y) \in \Omega_A, \tag{4.16}$$

$$\frac{\partial u_B}{\partial t} = \alpha_2 \nabla^2 u_B, \quad (x, y) \in \Omega_B. \tag{4.17}$$

External boundary conditions are the same as for single-layer material (Eqs (4.10)–(4.13)). At the common interface Γ_0 between two materials, temperature continuity and heat flux continuity conditions are satisfied:

$$u_j|_{\Gamma_0} = u_{j+1}|_{\Gamma_0}, \tag{4.18}$$

$$k_j \frac{\partial u_j}{\partial x}\bigg|_{\Gamma_0} = k_{j+1} \frac{\partial u_{j+1}}{\partial x}\bigg|_{\Gamma_0}. \tag{4.19}$$

Each layer has node density 11 × 201 (across the thickness × along the length), giving 21 × 201 nodes overall, with shape parameter $c = 0.36$ ($\beta = 72$).

Two features of Table 16 are worth noting. From $t = 1000$ s onward, the three deepest points differ by less than 0.25 °C because the steel layer occupying $0.05 \le x \le 0.10$ m has a diffusivity 44 times that of concrete and is therefore very nearly isothermal; the temperature drop is carried by the concrete layer. At $t = 200$ s, the two deepest points show undershoots of order 10^{-4} °C. These are above the double-precision floor and are the same boundary-stencil artefact quantified in Table 6; they amount to 10^{-6} of the temperature scale and do not affect any reported error norm, but we report them rather than suppress them.

Table 16. LRBFCM nodal temperatures (°C) of the two-layer wall, 4221 DOF. The monitoring abscissae are nodes of this grid ($h = 0.005$ m), so no interpolation is involved. The interface lies at $x = 0.05$ m.

t (s)	$x = 0.02$	$x = 0.04$	$x = 0.06$	$x = 0.08$	$x = 0.10$
200	11.808	0.25962	2.67×10^{-4}	-2.15×10^{-5}	-8.31×10^{-5}
1000	47.565	13.084	1.6900	1.5476	1.5005
5000	68.048	38.373	24.919	24.737	24.676
10000	77.652	56.887	47.469	47.342	47.300

Figure 14 presents the LRBFCM through-thickness profiles at $t = 200$, 1000, 2000, 5000, and 10000 s.

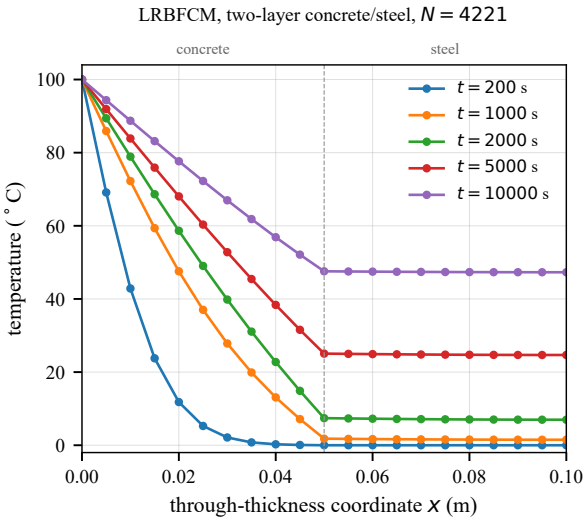

Figure 14. Through-thickness temperature profiles of the two-layer concrete/steel wall at the mid-length section, at $t = 200$, 1000, 2000, 5000, and 10000 s (4221 DOF). The broken line marks the material interface at $x = 0.05$ m; the steel layer is very nearly isothermal. Temperatures are in °C.

The interface treatment used for Figure 14 is also exercised in the separate steady interface-row check of Section 4.3, where it reproduces the analytical series-resistance profile of this configuration to 2.47×10^{-5} °C (Table 10).

4.7. Five-layer composite-wall heat conduction

The five-layer composite material consists of alternating materials A and B (A-B-A-B-A), each layer 0.02 m thick and 1 m long, forming a composite wall 0.1 m thick and 1 m long. Let Γ_j denote the interface between layers j and $j+1$. The four interface conditions are

$$u_j|_{\Gamma_j} = u_{j+1}|_{\Gamma_j}, \quad j = 1, 2, 3, 4, \tag{4.20}$$

$$k_j \frac{\partial u_j}{\partial x}\bigg|_{\Gamma_j} = k_{j+1} \frac{\partial u_{j+1}}{\partial x}\bigg|_{\Gamma_j}, \quad j = 1, 2, 3, 4. \tag{4.21}$$

Two material combinations are examined in this section.

4.7.1. Example 1: Concrete-structural steel composite material

Material A is concrete, and Material B is structural steel (parameters as in Section 4.6). Each sub-layer has node density 6×251 (across the thickness $\times$ along the length), i.e., 26×251 overall.

The pairs ($x = 0.02$, $x = 0.04$) and ($x = 0.06$, $x = 0.08$) of Table 17 bracket the two steel layers, and at every instant, the temperature difference across each pair is a small fraction of the drop across the adjacent concrete layer—0.39 against 25.2 °C at $t = 5000$ s, for instance. This is the behaviour required by the conductivity ratio of 84 and is consistent with the separate steady series-resistance check of Table 10.

Table 17. LRBFCM nodal temperatures (°C) of the five-layer concrete/steel wall, 6526 DOF. The monitoring abscissae coincide with the four interfaces and with the insulated face (h=0.004 m).

t (s)	$x = 0.02$	$x = 0.04$	$x = 0.06$	$x = 0.08$	$x = 0.10$
200	2.5887	2.1908	1.41×10^{-3}	7.36×10^{-4}	-4.13×10^{-6}
1000	24.371	23.789	2.5770	2.4629	0.74506
5000	61.116	60.726	35.503	35.326	31.433
10000	78.559	78.342	64.113	64.013	61.796

Figure 15 presents the LRBFCM through-thickness profiles at $t = 200$, 1000, 2000, 5000, and 10000 s.

Figure 15 shows that the temperature drop is carried almost entirely by the concrete layers, with the steel layers remaining very nearly isothermal, as expected from the conductivity ratio of 84. Table 10 gives the separate steady interface-row check for this configuration.

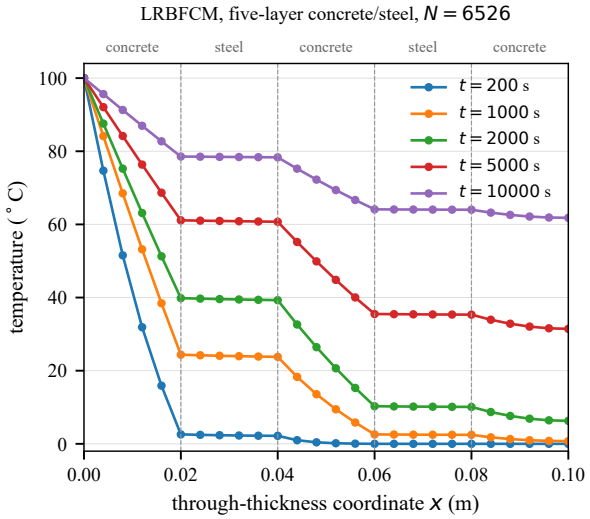

Figure 15. Through-thickness temperature profiles of the five-layer concrete/steel wall at the mid-length section at $t = 200$, 1000, 2000, 5000, and 10000 s (6526 DOF). Broken lines mark the four interfaces; the concrete layers carry essentially the whole temperature drop. Temperatures are in °C.

4.7.2. Example 2: Glass-air composite material

The second five-layer example illustrates the computed response for alternating glass and air layers. Material A is 0.02 m-thick glass: density $\rho_3 = 2500$ kg/m^3, thermal conductivity $k_3 = 1.4$ W/(m $\cdot^\circ$ C), specific heat capacity $c_{p3} = 750$ J/(kg $\cdot^\circ$ C), and thermal diffusivity $\alpha_3 = 7.47 \times 10^{-7}$ m^2/s. Material B is 0.02 m-thick air: density $\rho_4 = 1.16$ kg/m^3, thermal conductivity $k_4 = 0.026$ W/(m $\cdot^\circ$ C), specific heat capacity $c_{p4} = 1007$ J/(kg $\cdot^\circ$ C), and thermal diffusivity $\alpha_4 = 2.23 \times 10^{-5}$ m^2/s.

Figure 16 presents the LRBFCM through-thickness profiles at $t = 200$, 1000, 2000, 5000, and 10000 s.

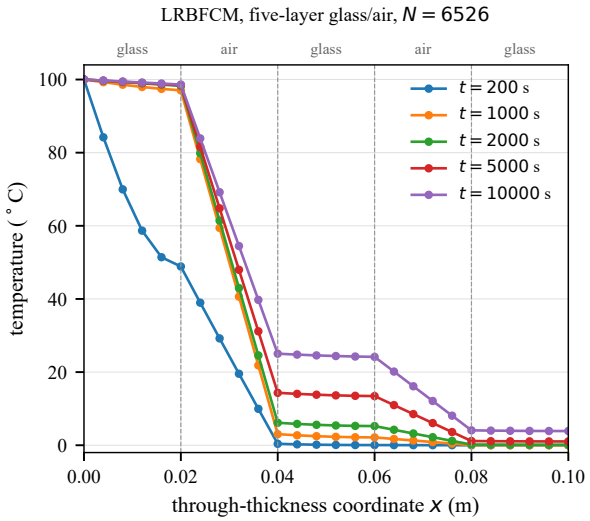

Figure 16. Through-thickness temperature profiles of the five-layer glass/air wall at the mid-length section at t = 200, 1000, 2000, 5000, and 10000 s (6526 DOF). The air layers, whose conductivity is 53.8 times lower than that of glass, carry almost the whole temperature drop, producing the staircase profile. Temperatures are in °C.

Table 18 quantifies the staircase: The drop across each glass layer is a small fraction of the drop across the adjacent air layer (0.87 °C across the glass layer between the second and third interfaces, against 73.6 °C across the air layer between the first and second, at t = 10000 s), as expected from the conductivity ratio of 53.8. Table 10 gives the separate steady interface-row check. All listed monitoring-point values are non-negative; this finite set of values is not, by itself, a global discrete maximum-principle test.

Table 18. LRBFCM nodal temperatures (°C) of the five-layer glass/air wall, 6526 DOF. The monitoring abscissae coincide with the four interfaces and with the insulated face (h=0.004 m).

t (s)	$x = 0.02$	$x = 0.04$	$x = 0.06$	$x = 0.08$	$x = 0.10$
200	48.874	0.39772	4.58×10^{-2}	2.41×10^{-4}	6.02×10^{-6}
1000	97.041	3.0332	2.1434	3.92×10^{-2}	2.08×10^{-2}
5000	98.430	14.337	13.442	1.1509	1.0376
10000	98.627	25.036	24.165	4.0718	3.8857

5. Conclusions and future work

This study reports calibration and verification of the LRBFCM for transient heat conduction in multilayer thin-walled media. It does not propose a new discretization principle. Its contribution is to document the parameter choices, state the discrete system explicitly, and verify the method against exact benchmarks and documented finite element runs.

On node distribution, the fixed-seed nonuniform cloud contains no duplicate nodes, yet its maximum local condition number rises from 3.77×10^6 at $c = 0.1$ to 1.01×10^{19} at $c = 5$. Its

best tested error, 2.69×10^{-1} at $c = 0.5$, is about two orders of magnitude larger than the corresponding uniform-grid result. This one realisation supports controlled near-uniform spacing but does not establish a distribution-free ranking. For second-kind boundary conditions, the direct method of Zheng et al. [25], applied with a consistent outward-normal convention, reduces the maximum boundary-test error from 5.43×10^{-4} to 6.89×10^{-5} in Section 3.2, a factor of 7.89 for that configuration. The size of the one-dimensional boundary stencil must, however, be kept small. Increasing it from $n_b = 3$ to $n_b = 9$ changes the magnitude of the insulated-face artefact by more than three orders for $\beta = 12$ and 20; at $\beta = 72$, the artefact changes sign, and the $n_b = 9$ case degrades the global error itself. The boundary-stencil findings are specific to the tested geometry, node set, and parameter values.

On the shape parameter, the favourable interval quoted for a 31×31 uniform distribution corresponds, in nondimensional form, to $27 \leq \beta \leq 75$ with $\beta = c/h$. The calibration of Section 3.4 shows that β^* grows as h^s with s between -0.63 and -0.91, so a fixed β is no more universal than a fixed c. On this fixed domain, c^*/L_x remains of order one, between 0.82 and 1.72 over the tested h and n_e. This suggests that the wall thickness is a relevant scale for the benchmark but does not establish a transferable geometric law. Each new domain therefore requires an error and conditioning check.

On the fixed single-layer node set and early-time window of Section 4.5, the usable $n_e = 9$ cases with $10 \leq \beta \leq 110$ produced no negative value above the stated floor. The usable $n_e = 13$ cases produced excursions of 0.12–0.38 °C. The selected wider-stencil setting has a smaller listed error. These results associate the early-excursion classification with stencil size in this sweep; they neither prove a global discrete maximum principle nor make the shape parameter irrelevant to accuracy. Among the usable $n_e = 9$ settings listed, $\beta = 72$ has the smallest error.

The single-layer example admits an exact series solution, and verification against it gives a spatial convergence rate of two on the coarser grids, degrading to about 1.2–1.4 on the finer grids at fixed β and fixed time step, together with the expected first-order temporal rate. A separate steady series-resistance calculation checks the interface rows and gives errors below 5×10^{-3} °C for conductivity ratios up to 84; it is not a transient multilayer benchmark.

In the controlled finite element tests, a substantial early-time undershoot (-14.4 to -14.6 °C in the listed cases) occurs with the eight-node quadratic formulation and not with the four-node linear formulation, and the listed changes to the mass-matrix and time-integration settings do not remove it. Rank et al. [31] provide a qualitative background on loss of discrete-maximum-principle behaviour for small time steps and consistent mass matrices. The observation is specific to the tested formulations and settings.

Table 14 reports paired later-time errors and early excursions for two selected LRBFCM settings, each obtained from independent constant-step runs starting from the same zero field. The $n_e = 9$, $\beta = 72$ setting has no observed undershoot above the numerical floor and an error of 2.321×10^{-2} K; the $n_e = 13, \beta = 33$ setting reduces the error to 2.065×10^{-3} K and has an early minimum of -1.175×10^{-1} °C. The FEM accuracy runs and early-time snapshots are listed separately in Table 15 because they do not form paired coordinates. No universal method-level ranking follows.

Future work includes developing an error-estimator-driven adaptive rule for β, so that the h-dependence identified here is handled automatically; extending the interface treatment to imperfect (contact-resistance) interfaces; and applying the scheme to three-dimensional and multiphysics problems.

Author contributions

Tao Ding and Yuanjian Lin: Conceptualization, Methodology, Validation, Visualization, Writing–original draft, and Writing–review and editing. Both authors have read and approved the final version of the manuscript.

Use of Generative-AI tools declaration

The authors used OpenAI Codex to assist with English-language editing, reference-format checking and LaTeX formatting. The authors reviewed all revisions and take full responsibility for the content. The tool was not used to generate or modify the research data, numerical results, figures or scientific conclusions.

Conflict of interest

All authors declare no conflicts of interest in this paper.

References

1. S. Q. Chen, C. H. Hu, J. J. Tian, D. W. Tan, Y. Q. Gong, F. Xia, et al., Voronoi cell finite element method for heat conduction analysis of composite materials, *Sci. Rep.*, **14** (2024), 12083. https://doi.org/10.1038/s41598-024-61263-4
2. V. S. Suvin, E. T. Ooi, C. Song, S. Natarajan, Temperature-dependent nonlinear transient heat conduction using the scaled boundary finite element method, *Int. J. Heat Mass Tran.*, **243** (2025), 126780. https://doi.org/10.1016/j.ijheatmasstransfer.2025.126780
3. Y. R. Yuan, C. F. Li, H. L. Song, An upwind-block-centered finite difference method for a semiconductor device of heat conduction and its numerical analysis, *J. Comput. Appl. Math.*, **425** (2023), 114978. https://doi.org/10.1016/j.cam.2022.114978
4. E. J. Kansa, Multiquadrics—a scattered data approximation scheme with applications to computational fluid dynamics—I: surface approximations and partial derivative estimates, *Comput. Math. Appl.*, **19** (1990), 127–145. https://doi.org/10.1016/0898-1221(90)90270-T
5. E. J. Kansa, Multiquadrics—a scattered data approximation scheme with applications to computational fluid dynamics—II: solutions to parabolic, hyperbolic and elliptic partial differential equations, *Comput. Math. Appl.*, **19** (1990), 147–161. https://doi.org/10.1016/0898-1221(90)90271-K
6. W. R. Madych, S. A. Nelson, Multivariate interpolation and conditionally positive definite functions, II, *Math. Comp.*, **54** (1990), 211–230. https://doi.org/10.1090/S0025-5718-1990-0993931-7
7. C. A. Micchelli, Interpolation of scattered data: distance matrices and conditionally positive definite functions, *Constr. Approx.*, **2** (1986), 11–22. https://doi.org/10.1007/BF01893414
8. X. Zhang, K. Z. Song, M. W. Lu, X. Liu, Meshless methods based on collocation with radial basis functions, *Comput. Mech.*, **26** (2000), 333–343. https://doi.org/10.1007/s004660000181

9. W. Chen, New RBF collocation methods and kernel RBF with applications, In: *Meshfree methods for partial differential equations*, Berlin: Springer, 2003, 75–86. https://doi.org/10.1007/978-3-642-56103-0_6

10. B. Fornberg, N. Flyer, Solving PDEs with radial basis functions, *Acta Numer.*, **24** (2015), 215–258. https://doi.org/10.1017/S0962492914000130

11. B. Šarler, R. Vertnik, Meshfree explicit local radial basis function collocation method for diffusion problems, *Comput. Math. Appl.*, **51** (2006), 1269–1282. https://doi.org/10.1016/j.camwa.2006.04.013

12. R. Vertnik, B. Šarler, Meshless local radial basis function collocation method for convective-diffusive solid-liquid phase change problems, *Int. J. Numer. Method. H.*, **16** (2006), 617–640. https://doi.org/10.1108/09615530610669148

13. C. Z. Shi, H. Zheng, P. H. Wen, Y. C. Hon, The local radial basis function collocation method for elastic wave propagation analysis in a 2D composite plate, *Eng. Anal. Bound. Elem.*, **150** (2023), 571–582. https://doi.org/10.1016/j.enganabound.2023.02.021

14. P. F. Jiang, H. Zheng, J. G. Xiong, C. Z. Zhang, A stabilized local RBF collocation method for incompressible Navier-Stokes equations, *Comput. Fluids*, **265** (2023), 105988. https://doi.org/10.1016/j.compfluid.2023.105988

15. A. Yazdani, F. Fakhar-Izadi, M. Abbaszadeh, Adaptive radial basis function collocation method for elliptic interface problems, *Eng. Anal. Bound. Elem.*, **179** (2025), 106420. https://doi.org/10.1016/j.enganabound.2025.106420

16. X. B. Yan, H. Zheng, D. J. Yan, Analysis of the band structure of transient in-plane elastic waves based on the localized radial basis function collocation method, *Appl. Math. Model.*, **125** (2024), 468–484. https://doi.org/10.1016/j.apm.2023.09.002

17. P. F. Jiang, H. Zheng, J. G. Xiong, T. Rabczuk, The localized radial basis function collocation method for dendritic solidification, solid phase sintering and wetting phenomena based on a phase-field model, *J. Comput. Phys.*, **520** (2025), 113515. https://doi.org/10.1016/j.jcp.2024.113515

18. Y. K. Wang, X. H. Jing, L. Qiu, Localized radial basis function collocation method for long-time simulation of nonlinear transient heat conduction problems, *Appl. Math. Lett.*, **165** (2025), 109525. https://doi.org/10.1016/j.aml.2025.109525

19. L. Qiu, F. J. Wang, Y. Gu, Q. H. Qin, Modified space-time radial basis function collocation method for long-time simulation of transient heat conduction in 3D anisotropic composite materials, *Int. J. Numer. Meth. Eng.*, **124** (2023), 4639–4658. https://doi.org/10.1002/nme.7327

20. J. Y. Wang, L. Qiu, Y. J. Liang, F. J. Wang, A spatio-temporal radial basis function collocation method based on Hausdorff fractal distance for Hausdorff derivative heat conduction equations in three-dimensional anisotropic materials, *Appl. Math. Comput.*, **502** (2025), 129501. https://doi.org/10.1016/j.amc.2025.129501

21. X. H. Jing, L. Qiu, H. Zhao, Z. Q. Zhang, Y. M. Zhang, Y. Gu, An accurate and stable space-time radial basis function collocation method for transient coupled thermo-mechanical analysis, *J. Comput. Sci.*, **92** (2025), 102720. https://doi.org/10.1016/j.jocs.2025.102720

22. X. K. Li, S. D. Zhao, W. Z. Qu, Localized Fourier collocation method for 2D transient heat conduction problems, *Appl. Math. Lett.*, **160** (2025), 109331. https://doi.org/10.1016/j.aml.2024.109331

23. W. X. Sun, W. Z. Qu, Y. Gu, P. W. Li, An arbitrary-order numerical framework for transient heat conduction problems, *Int. J. Heat Mass Tran.*, **218** (2024), 124798. https://doi.org/10.1016/j.ijheatmasstransfer.2023.124798

24. W. X. Sun, H. D. Ma, W. Z. Qu, A hybrid numerical method for nonlinear transient heat conduction problems with temperature-dependent thermal conductivity, *Appl. Math. Lett.*, **148** (2024), 108868. https://doi.org/10.1016/j.aml.2023.108868

25. H. Zheng, C. Z. Zhang, Y. S. Wang, J. Sladek, V. Sladek, A meshfree local RBF collocation method for anti-plane transverse elastic wave propagation analysis in 2D phononic crystals, *J. Comput. Phys.*, **305** (2016), 997–1014. https://doi.org/10.1016/j.jcp.2015.10.020

26. H. Zheng, Z. Yang, C. Zhang, M. Tyrer, A local radial basis function collocation method for band structure computation of phononic crystals with scatterers of arbitrary geometry, *Appl. Math. Model.*, **60** (2018), 447–459. https://doi.org/10.1016/j.apm.2018.03.023

27. S. Rippa, An algorithm for selecting a good value for the parameter c in radial basis function interpolation, *Adv. Comput. Math.*, **11** (1999), 193–210. https://doi.org/10.1023/A:1018975909870

28. G. E. Fasshauer, J. G. Zhang, On choosing "optimal" shape parameters for RBF approximation, *Numer. Algor.*, **45** (2007), 345–368. https://doi.org/10.1007/s11075-007-9072-8

29. R. Schaback, Error estimates and condition numbers for radial basis function interpolation, *Adv. Comput. Math.*, **3** (1995), 251–264. https://doi.org/10.1007/BF02432002

30. H. Zheng, G. M. Yao, L. H. Kuo, X. X. Li, On the selection of a good shape parameter of the localized method of approximated particular solutions, *Adv. Appl. Math. Mech.*, **10** (2018), 896–911. https://doi.org/10.4208/aamm.OA-2017-0167

31. E. Rank, C. Katz, H. Werner, On the importance of the discrete maximum principle in transient analysis using finite element methods, *Int. J. Numer. Meth. Eng.*, **19** (1983), 1771–1782. https://doi.org/10.1002/nme.1620191205

AIMS Press